Passive Micron-scale Time-of-Flight with Sunlight Interferometry

ALANKAR KOTWAL, Carnegie Mellon University

ANAT LEVIN, Technion

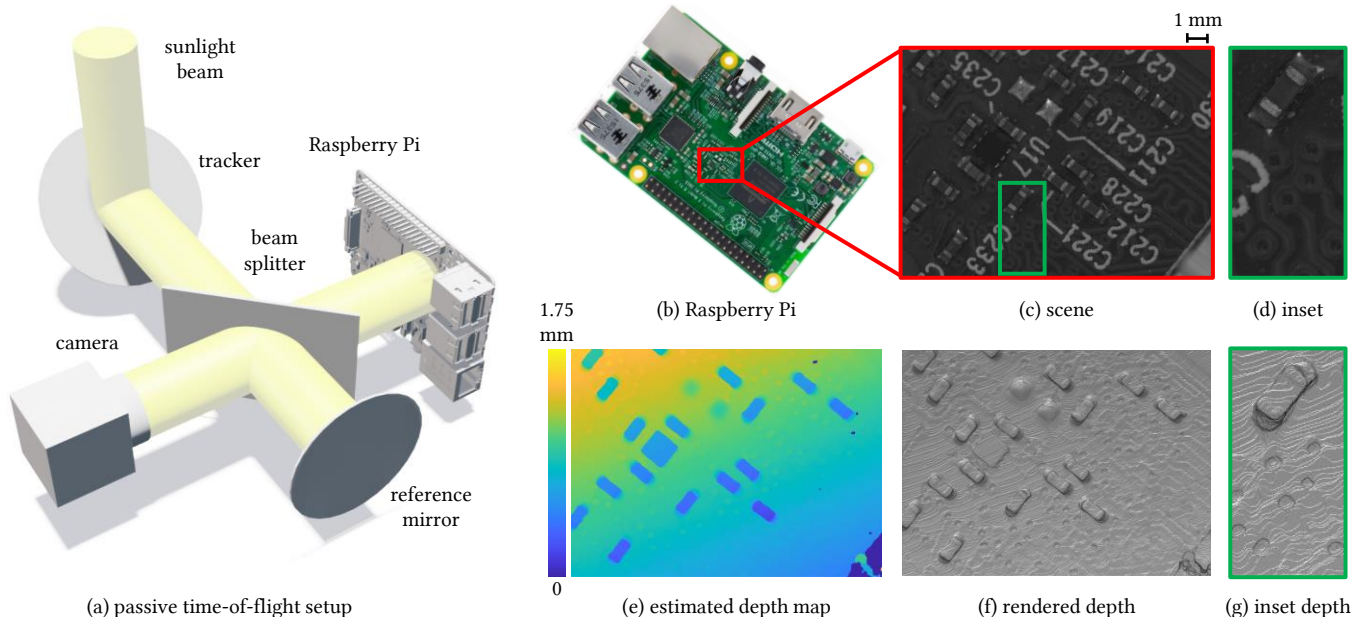IOANNIS GKIOULEKAS, Carnegie Mellon University

Fig. 1. **Reconstructing a part of the Raspberry Pi circuit board**. **(a)** Schematic of the passive interferometric time-of-flight system. **(b)** We reconstruct a part of the Raspberry Pi circuit board that has multiple resistors, soldering pads and tracks. **(c)** A picture of the scene as seen through the imaging camera, **(d)** scene image cropped to the green rectangle in (c), **(e)** the depth estimated by passive interferometry shown as an image, **(f)** rendered as a surface, and **(g)** cropped to (d). Note the exquisite detail in the depth along the PCB tracks and in the through-holes.

Recovering depth maps of 3D objects is a central focus of research in computer vision and computational imaging. The depth sensing methods yielding the highest-quality results available today are active illumination methods such as structured light and time-of-flight. However, most active illumination methods fail under the strong ambient light conditions typically found outdoors. Passive depth sensing methods, that use the ambient light for signal, therefore have the advantage outdoors. Passive methods also consume lesser power due to the absence of the projector system. However, traditional passive methods yield millimeter-scale axial resolution at best. In addition, passive methods are susceptible to the adverse effects of global illumination caused by multibounce light transport and fail in the presence of strong subsurface scattering and interreflections in the scene.

The best techniques for micron-scale depth sensing are based on interferometry. Interferometry, when done with spatially and temporally incoherent light, can produce high spatial- and axial-resolution depth maps robust to global illumination. Here, we combine the advantages of passive techniques, the micron-scale resolution of interferometry and the inherent incoherence of everyday light sources like the sun to perform passive, micron-scale depth sensing. The robustness to global illumination also gives us the ability to perform seeing through optically-thin scattering media with everyday light sources. We show how to design an interferometric setup that avoids the usual detriments to using interferometry outside the lab, such as vibrations and wind. Our results for depth sensing and seeing through scattering exhibit the strong potential of passsive interferometry for outdoor applications.

1 INTRODUCTION

Depth sensing is a vital part of many applications in a variety of fields such as robotics, human-computer interactions and biomedical imaging. Therefore, recovering the 3D shape of objects has been an important focus of research in computer vision for many decades. The earliest depth sensing methods are *passive* in nature: They rely on external light to illuminate the scene and provide signal to the camera. Upon imaging, this light gives rise to cues such as disparity in images from multiple cameras [Barnard and Thompson 1980; Hartley and Zisserman 2004; Nalpantidis et al. 2008], interreflections [Nayar et al. 1990], focus [Grossmann 1987; Hasinoff and Kutulakos 2006; Hazirbas et al. 2018; Subbarao and Surya 1994] and shading [Han et al. 2013; Horn 1970], all of which can be exploited for depth sensing. However, the existence and utility of these cues make strong assumptions on the nature of the scene (texture for disparity, BRDF models for shading and so on), and cannot be used when these assumptions are violated. These limitations are partially removed in *active* imaging techniques that project light coded in some way: Either spatially, so as to artificially create these cues [Chen et al. 2008; Gupta et al. 2011; O'Toole et al. 2015, 2016; Scharstein and Szeliski 2003; Woodham 1980; Zickler et al. 2002], temporally so as to obtain per-pixel depth-dependent measurements [Aull 2005;

Gariepy et al. 2015; Gupta et al. 2019a,b; Heide et al. 2018, 2013; Kirmani et al. 2009, 2014; Lange and Seitz 2001; Lange et al. 2000; Lindell et al. 2018; Niclass et al. 2005; O'Toole et al. 2017; Piatti et al. 2013; Rochas et al. 2003; Schwarte et al. 1997; Velten et al. 2012; Villa et al. 2014], or combinations thereof [Achar et al. 2017]. However, with a few exceptions [Achar et al. 2017; O'Toole et al. 2015], active depth sensing fails under strong ambient lighting conditions that overwhelm the projected illumination. Passive sensing techniques, then, remain the methods of choice for depth sensing under strong ambient light. Passive depth sensing techniques also consume lesser power than active ones, a strong benefit in mobile applications.

Micrometer-scale depth resolution evades both these classes of depth sensing methods because of various limitations of the hardware and algorithms used. For instance, time-of-flight techniques are constrained to millimeter-scale resolution due to the declining response of electronics to frequencies above 100 MHz [Baek et al. 2021], corresponding to a millimeter-scale resolution. The only depth sensing methods that achieve reliable, physically-guaranteed micron-scale resolution (including ours in this article) are based on interferometry. However, the micron-scale sensitivity of interferometry makes it notoriously sensitive to environmental conditions such as vibrations and wind, apparently preventing its use in outdoor conditions. At present, most applications of optical interferometry are restricted to controlled conditions in the lab [Cheng and Wyant 1984, 1985; de Groot 2011; de Groot and McGarvey 1992; Fercher et al. 1985; Gkioulekas et al. 2015; Houairi and Cassaing 2009; Huang et al. 1991; Johnson et al. 2001; Kotwal et al. 2020; Li et al. 2018, 2017; Lu and Lee 2002; Meiners-Hagen et al. 2009; Yan et al. 2015]. In addition, interferometry is an active illumination technique that is susceptible to the same ambient light issues as above.

Interferometric methods share with traditional depth reconstruction methods the inability to handle global illumination caused by multi-bouce light transport. Global illumination introduces spurious signal into measurements with either of these methods, rendering depths in scenes with especially strong interreflections or subsurface scattering inaccurate. Kotwal et al. [2020] introduced an interferometric method for *probing* light transport that, among other capabilities, has the ability to reject most global illumination from interferometric measurements using *spatially incoherent* illumination. Combined with the optical coherence tomography technique of Huang et al. [1991] (that uses *temporally incoherent* light), their technique can yield high spatial- and axial-resolution depth maps of scenes with complicated multi-bounce light transport.

We present a *passive* interferometric method that uses light from everyday sources, such as the sun and indoor lamps, to recover depth maps at micron spatial and axial resolutions. We prove that such illumination is inherently spatially and temporally incoherent, making the above depth recovery robust to most global illumination. We engineer an optical setup that we demonstrate to be robust to most detrimental environmental factors. The depth sensing and seeing through scattering results from this setup show the potential of interferometry performed passively with ambient light.

Passive interferometry has been extensively explored in the context of seismology [Claerbout 1968; Draganov and Ruigrok 2015; Schuster 2009] for subsurface imaging. Similar approaches had been

used in ultrasound imaging [Weaver and Lobkis 2001]. These methods show that cross-correlations of the responses of sensors to noise signals provides a passive means to measure the problem-specific Green's function between the two sensors. This idea was extended to obtain temporally-resolved measurements of Green's functions through thick scattering materials in optics by Badon et al. [2015, 2016]; Davy et al. [2013] using a Michelson interferometer. Recently, passive localization of light sources has been achieved using cross-correlations of light scattered by diffusive barriers [Batarseh et al. 2018; Boger-Lombard and Katz 2019] for seeing through scattering and non-line-of-sight imaging.

In radio astronomy, passive interferometry is a means of imaging astronomically distant light sources using their emitted light [Jennison 1958]. Brown and Twiss [1954, 1956] introduced an interferometer design to measure the angular diameter of radio light sources. The interferometer they proposed has been extended to *very-long-baseline interferometry*, which has been used extensively to perform high-resolution imaging of cosmic radio sources such as the recent result that produced first-ever image of a black hole [Akiyama et al. 2019; Bouman et al. 2016].

In contrast to these methods, our method measures a restriction of the scene Green's function to a planar surface placed at the focal distance of the imaging camera, called the *transmission function*. We show that these measurements are a slice of the transmission function that is invariant to the effects of most global illumination. We postulate that this measurement is sufficient to yield micron-scale time-of-flight information robust to global illumination. We relate this time-of-flight information to the depth of the scene point closest to the camera for sufficiently diffuse scenes, thus yielding micron-scale depth sensing. In scenes with significant optically-thin scattering, we show that the invariance of the measurement to global illumination yields a passive method for seeing through scattering under strong ambient light.

In the same way as Kotwal et al. [2020] generalize the insights of Gkioulekas et al. [2015] to perform interferometric computational light transport, we envision future research generalizing the concept developed in this article to develop *passive* interferometric computational light transport. We hope that this passive means of measuring transmission matrices will extend to applications such as seeing through scattering [Bertolotti et al. 2012; Kim et al. 2015; Metzler et al. 2017; Popoff et al. 2010a,b; Sharma et al. 2019], temporal focusing through scattering media [Kim et al. 2015; Mosk et al. 2012; Vellekoop and Mosk 2007] and enhancing energy delivery through media [Kim et al. 2015; Vellekoop and Mosk 2008].

2 METHOD

Our setup is a modified version of the classical full-field Michelson interferometer [Hariharan 2003], as shown in Figure 2(b). The interferometer splits the input light beam into two 'arms': One propagating towards the scene of interest, and one towards a reference arm, which is typically a planar mirror the distance l of which to the beam splitter can be controlled with a translation stage. A camera then measures the superposition of light reflected from both arms. Instead of the artificially created light source a traditional Michelson interferometer uses, our setup uses extended and broadband
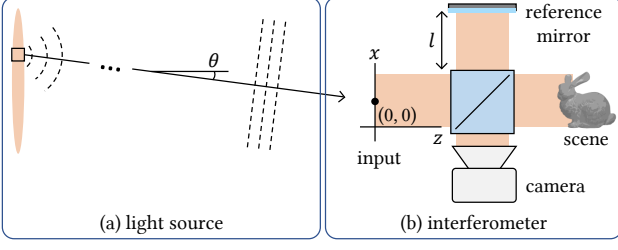
Fig. 2. **(a)** We use light from commonly-available light sources around us, such as the sun and indoor lights, as illumination to perform passive depth sensing. We assume that these light sources are far enough for their light to be considered a collection of plane waves near the optical axis of our imaging system. **(b)** We inject this light into a classical full-field Michelson interferometer. The interferometer superimposes on the camera the response of the scene to the input illumination and light returning from a reference arm that applies a constant phase shift to the entire beam. Interferometry with such *spatially and temporally incoherent* illumination can perform high-quality, micrometer-resolution depth sensing.

ambient light sources, such as the sun or indoor lamps, as shown in Figure 2(a), to perform micron-scale depth sensing.

We will now describe the wave field created at the input of the interferometer by such an extended light source placed in the far-field. We assume that the source is distant enough for the entire of the emitted light to be modeled as a wave field of independently emitting point sources over a plane. Then, each point on the source emits a diverging spherical wave field towards the interferometer input. When the light source is sufficiently far from the input, we can approximate this emitted field paraxially as a plane wave propagating at an angle θ to the optical axis, as shown in Figure 2(a). Referring to the coordinate system in Figure 2(b), such a wave field at optical wavelength λ is given by the phasor expression

$$u^{\theta}(x, z) = \exp(-i\kappa(x\theta + z)) \qquad (1)$$

where $\kappa \equiv 2\pi/\lambda$ is the wavenumber. The total wave field created at the input is a sum over input angles θ and source spectrum κ, with the different components being fully incoherent with each other.

Such illumination spanning a set of angles θ has been shown to be *spatially incoherent* by Gkioulekas et al. [2015], which makes interferometry using such illumination robust to most global illumination. In addition, the broadband spectrum offers *temporal incoherence*, giving us the ability to measure light paths based on the length they travel in the scene. To formalize this, we will quote a result from Kotwal et al. [2020], which gives the interference measurement in terms of the coherence properties of the illumination and the distance l from the beamsplitter to the reference mirror:

$$\text{corr}(x, l) = \int_{x', \tau} \mathcal{T}^c(x, x', \tau) G(c\tau - l) S(x - x') \, d\tau \, dx', \qquad (2)$$

where $\mathcal{T}^c(x, x', \tau)$ is the *pathlength-resolved light transmission function* of the scene, describing the coherent interaction of light with the scene, $G(c\tau - l)$ is the *temporal coherence function* and $S(x - x')$ is the *spatial coherence kernel*. As Gkioulekas et al. [2015] point out, the spatial coherence function $S(x - x')$ is sharply peaked for a source sufficiently wide in θ: $S(x - x') \approx \delta(x - x')$. In addition, the temporal coherence function $G(c\tau - l)$, for broadband illumination, is sharply-peaked: $G(c\tau - l) \approx \delta(c\tau - l)$. This implies that for a

sufficient large and broadband source, the interference measures

$$\text{corr}(x, l) = \mathcal{T}^c(x, x, l), \qquad (3)$$

which is the component of scene appearance arising from *ballistic* light paths (the ones arising at point x and terminating at point x as well) having traveled a pathlength l in the scene. This scene appearance is invariant to light paths caused by global illumination, the overwhelming majority of which end up at x' for $x \neq x'$. For sufficiently diffuse scenes, we can assume all ballistic light paths to have reflected off of the surface of the scene closest to the beamsplitter. Then, the depth of any point on the scene is the position l of the reference mirror where the interference signal is the maximum.

Our method has a slightly counter-intuitive and unique property. As we mention above, making our light source increasingly incoherent enables increasingly high spatial- and axial-resolution imaging. This requires us to broaden the light source in size θ and in spectrum κ. However, choosing a bigger source and broadening its spectrum lets more light into the scene, thus increasing the signal-to-noise ratio of the intensity measurements we take. The resolutions of our method are then theoretically only limited by our ability to position the translation stage accurately and the pixel size of the camera. In contrast, most computational imaging approaches trade SNR in intensity measurements off with improvement in performance over traditional imaging techniques [Cossairt 2011, Chapter 5].

Hardware setup. We illustrate the hardware setup we built for passive interferometry in Figure 3. To bring the setup outside the lab, we built it on an ordinary utility cart. Since it is not practical to orient the optical axis of the interferometer towards the selected source of light, we installed a tracking assembly shown in the green boxes in Figure 3. This assembly consists of a mirror whose 3D orientation can be controlled via two motorized rotation stages. We set the orientation of the mirror by imaging the light source through a camera whose lens is focused on the source (or infinity, for a source sufficiently far away) so that the source appears in the center of the field of view. This guarantees that the tracking mirror deflects light from the source parallel to the optical axis of the system. To mitigate the effects of vibrations, we placed the entire optical setup on a passively-damped optical breadboard. Following the tracking assembly is a standard full-field Michelson interferometer. For full details of the setup, please refer to the supplementary material.

Post-processing. Upon capturing a stack of intensity measurements at a dense set of reference arm positions l using the setup (Figure 4(a)), we need to post-process them to extract interference measurements. We will denote the $H \times W \times N$ stack of intensity measurements I_n where n goes from 1 to n. We will denote the set of corresponding reference arm positions as l_n. Then, we estimate the set of interference-free images $\tilde{I}_n$ at every position by performing an average over a window of t frames around the position (Figure 4(b)):
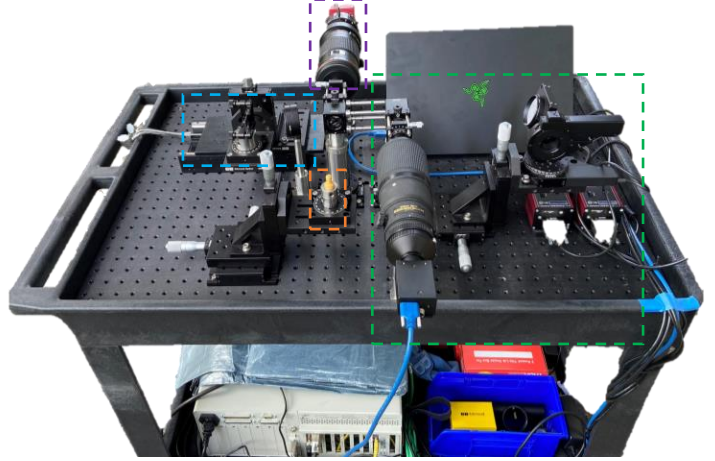
$$\tilde{I} = I * \mathbf{1}_t, \qquad (4)$$

where $\mathbf{1}_t$ is a $1 \times 1 \times t$ array of ones and $*$ represents an N-dimensional convolution operation. Then, we subtract the interference-free images from the intensity measurements to obtain interference-only images $\tilde{C}_n$ (Figure 4(c)):

$$\tilde{C}_n = |I_n - \tilde{I}_n|. \qquad (5)$$
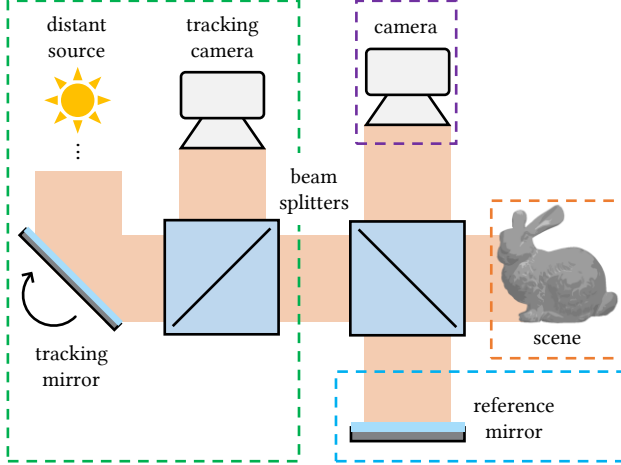
Fig. 3. **(a)** Schematic and **(b)** physical prototype of the passive interferometry setup. In order to be able to do interferometry outdoors, we build the optical setup on a passively-damped breadboard placed on an ordinary utility cart. We use a tracking assembly that uses a mirror whose position is controlled with a closed-loop system to inject ambient light into the interferometer, as shown in the green box.
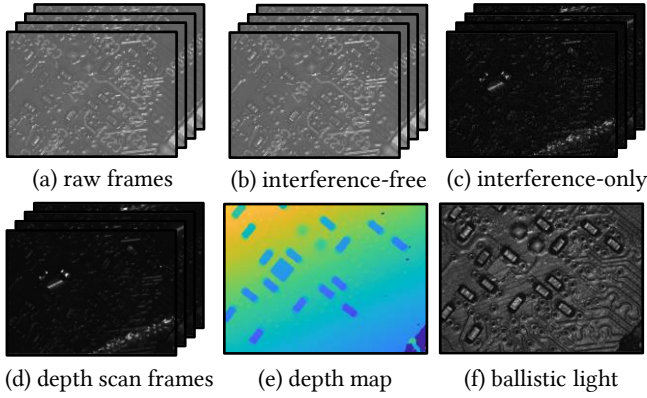

Fig. 4. **Processing pipeline to get direct-only and depth images**. **(a)** We capture a stack of images with the reference arm placed at a dense set of positions, **(b)** we blur the stack temporally to estimate interference-free images, **(c)** we subtract interference-free images from the captured images to get interference-only images, **(d)** we spatially blur the interference-only images, **(e)** calculate direct-only images as the maxima of the interference-only images and **(f)** the depth as the reference arm position at these maxima.

We then blur, channel-wise, the interference to yield the final correlation measurements of Equation 3 (Figure 4(d)):

$$C = \tilde{C} * \mathcal{G}_s, \tag{6}$$

where $\mathcal{G}_s$ is an appropriately-sized Gaussian kernel with standard deviation of s pixels.

Finally, we estimate depth of pixel p as the position of the maximum of the correlation measurement for pixel p (Figure 4(e)):

$$d(p) = l_{\operatorname*{argmax}_n C_n(p)}, \tag{7}$$

where we have made the dependence of the correlation on pixels p explicit. We then process this estimated depth using standard denoising approaches such as the median filter to yield a final depth map. We estimate the image of ballistic light as the per-pixel maximum

of the correlation measurement (Figure 4(f)):

$$D(p) = \max_n C_n(p). \tag{8}$$

3 RESULTS

Results with sunlight. We test the passive interferometry setup using sunlight on a variety of scenes in Figure 5. These scenes pose challenges including low signal intensity (circuit board), specularities (coin and pawn) and strong subsurface scattering (chocolate, soap and pill). In addition, there are challenges posed by the location and environmental conditions of the capture, which we explain in the supplementary material. The quality of the recovered depths even in the presence of these challenges shows the potential of passive interferometry using sunlight.

Result with indoor light. Figure 6 shows the coin scene from Figure 5 reconstructed using an ordinary desk lamp placed about five feet from the tracking mirror. Even though five feet isn't in the far-field of the interferometer input, we obtain depth with quality comparable to the depth recovered with sunlight. Unfortunately, this depth measurement is currently possible for us only for specular scenes like the coin, because the lamp does not emit enough light to get any signal from diffuse scenes without impractically large exposure times. In addition, being in the near-field, every source point presents a quadratic phase profile across the illumination, distorting depth acquisition. The distortion isn't apparent in this result because of the strong tilt of the coin to the optical axis.

Seeing through scattering media with sunlight. Kotwal et al. [2020] demonstrated seeing through scattering media using spatially incoherent illumination to measure only ballistic light paths. Since our illumination is inherently spatially incoherent, in addition to depth acquisition, we can also attempt to perform seeing through scattering. Figure 7 shows the coin scene from Figure 5 viewed under three increasingly challenging conditions: (a) with the coin facing
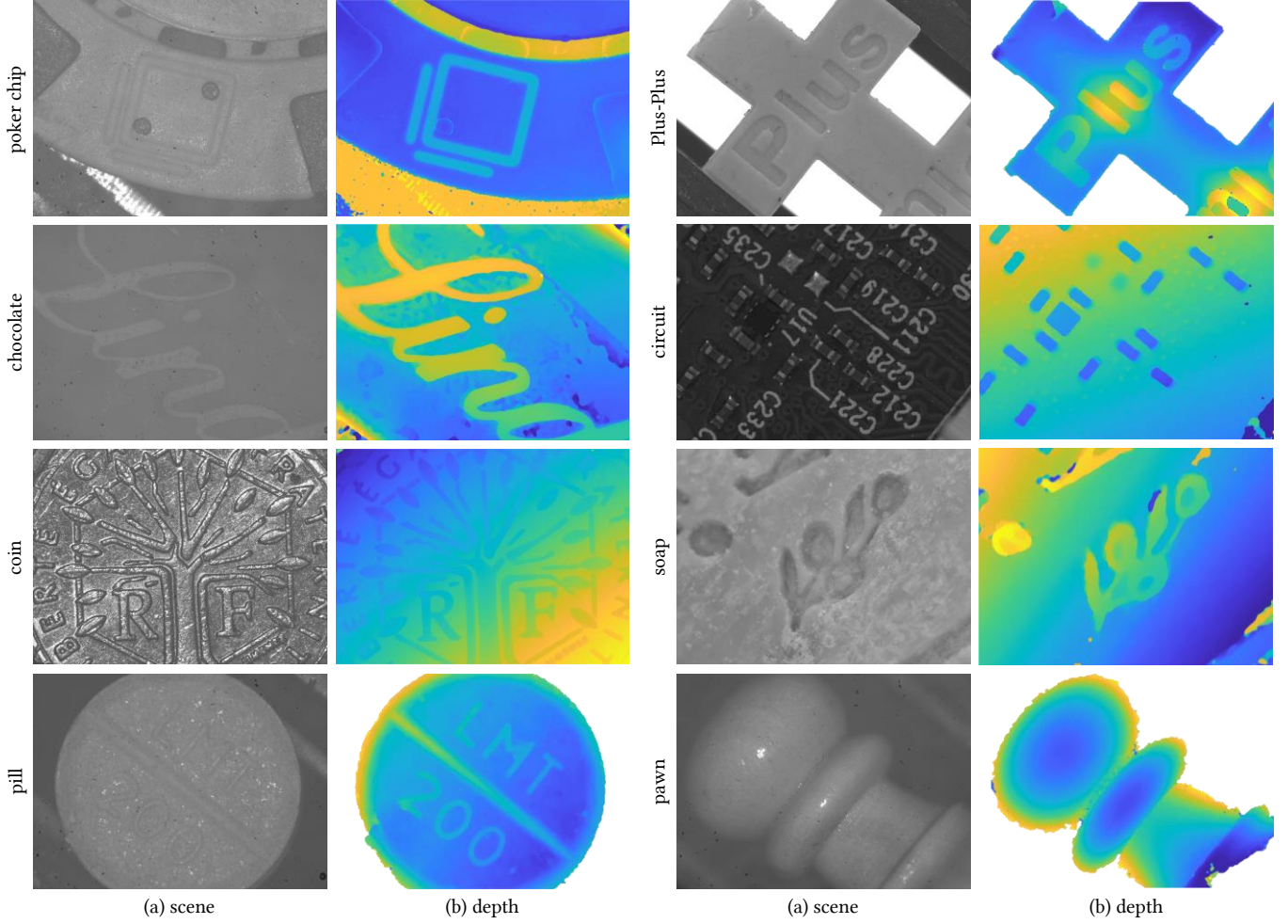
Fig. 5. **Micron-scale depth reconstructions for a variety of challenging scenes using sunlight**. The challenges include vibrations caused due to various factors in the acquisition location (that we discuss in the supplement), strong sub-surface scattering in the chocolate, pill and soap, specularities in the coin and pawn, and low intensity in the circuit board.
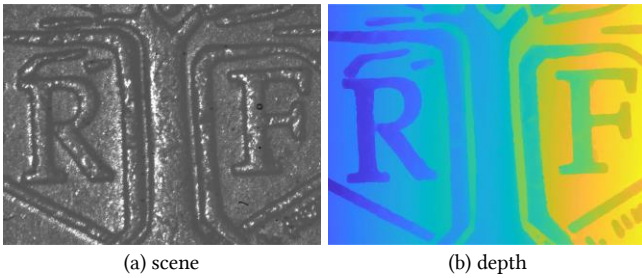

Fig. 6. **Micron-scale depth reconstruction using light from an ordinary desk lamp** illuminating the scene from about five feet. Even though the lamp isn't in the far-field of the interferometer, we get depth with reasonable quality. This depth has a quadratic distortion that isn't apparent because of the strong tilt of the coin to the optical axis.

the camera directly, (b) with a 200-grit ground glass diffuser stuck to it, and (c) the diffuser placed at 4 mm from the coin. The presence of the diffuser causes significant light scattering in the path of light

to the coin, and images of the scene with the diffuser are blurred to the point that (c) does not show any fine detail on the coin at all.

The inherent incoherent nature of our illumination gives us the ability to reject in the measured interference component the scattered part of scene appearance that contributes to global illumination, and therefore lets us see through scattering media. We observe in the fourth row that under all three conditions, the interference component we measure is free from this scattering and recovers all the fine details lost in the scene image. In addition, we are able to measure a depth map of the coin through the scatterer, albeit lower in quality due to the lost interference signal quality.

Coherence characteristics of sunlight. The spatial and axial resolutions of our depth sensing system depend on the coherence characteristics of light. As Equation 2 suggests, the wider the spatial coherence kernel $S(x - x')$ and the temporal coherence function $G(c\tau - l)$, the farther the measurement departs from Equation 3.
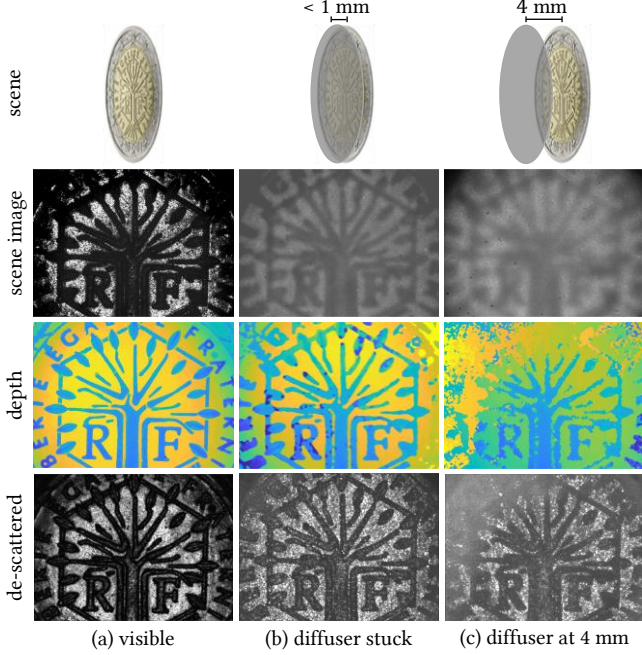
Fig. 7. **Seeing through scattering with spatial incoherence**. This experiment images the coin under three increasingly challenging conditions: **(a)** directly, **(b)** with a ground glass diffuser stuck to the coin and **(c)** with the diffuser at 4 mm from the coin. The diffuser causes images of the scene taken by the camera to be blurred. In contrast, the interference component measures only ballistic light, rejecting scattering and de-blurring the images. We can also estimate a depth map of the coin through the scattering, albeit at a lower quality due to the lost interference signal.
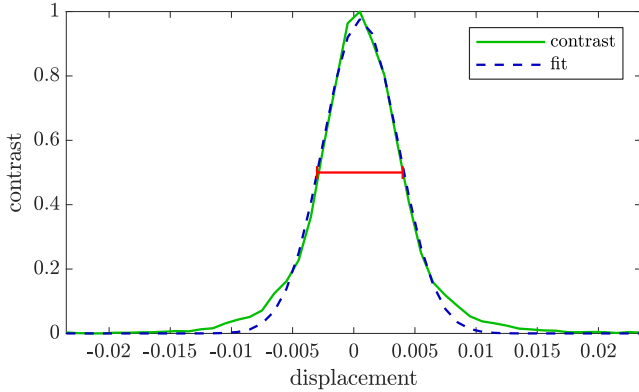

Fig. 8. **Measuring the temporal coherence length of sunlight with a 550±20 nm spectral filter**. We place a mirror as the scene, measure interference for a dense set of reference positions and plot the variance of the measurements as a function of position to get the temporal coherence function. The full width at half-maximum of a Gaussian fit to this function is around 10 μm, validating our claim of micron-scale resolution.

Specifically, the wider the temporal coherence function $G(c\tau - l)$, the more light with $c\tau \neq l$ is allowed into the interference, decreasing axial resolution. To determine the axial resolution, we measure the temporal coherence function of sunlight with a 550±20 nm filter in Figure 8(a). We place a mirror on the scene arm, capture
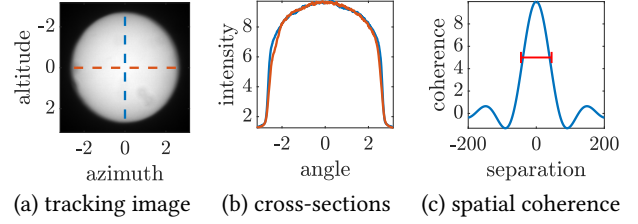

(a) tracking image   (b) cross-sections   (c) spatial coherence

Fig. 9. **Measuring the angular extent of the sun to estimate the spatial coherence area of sunlight**. **(a)** An image of the sun captured on the tracking camera. The units on the axes are in units of 0.1 degrees. **(b)** Plots of the vertical and horizontal cross-sections through the center of the sun image. This plot yields an approximate angular extent of 0.57° for the sun. **(c)** The van Cittert-Zernike theorem yields for such a source the spatial coherence kernel specified by Equation 9, which is plotted here. The x-axis is in units of 0.1 degrees. The full-width at half-maximum of this kernel, representing the spatial coherence length, is around 100 μm.

measurements at a dense set of positions of the reference arm, and plot the variance of the measurements versus position. The full-width at half-maximum of a Gaussian fit, or the *temporal coherence length*, is 10 μm, validating our claim of micron-scale resolution.

In analogy, the wider the spatial coherence kernel $S(x - x')$, the more light from neighboring points x' with $x \neq x'$ is allowed into the interference measurement, effectively decreasing the robustness to global illumination and spatially blurring the depth estimate. To quantify the width of the spatial coherence kernel, or the *spatial coherence length*, we can use the van Cittert-Zernike theorem [Born et al. 1999, Section 10.4.2] on the angular extent of the sun. We estimate, in Figure 9, the angular extent of the sun to be around 0.57°. The spatial coherence kernel of a distant, uniform, incoherent light source with angular extent ϕ is given by [Deng and Chu 2017]

$$S(\Delta x) = \frac{J_1(\pi \Delta x \phi / \lambda)}{\pi \Delta x \phi / \lambda}, \tag{9}$$

where $J_1(\cdot)$ is the Bessel function of the first kind, first order. This is plotted in Figure 9(d). This kernel yields a spatial coherence length of the order of 100 μm, consistent with the theoretical estimate by Agarwal et al. [2004] and measurement by Mashaal et al. [2012].

4 CONCLUSION

In conclusion, we have demonstrated a passive interferometric method for micron-scale depth sensing outside the controlled environment of the lab. Using light from ambient sources such as the sun mitigated the need to use expensive, power-hungry, high-power or eye-unsafe lasers for interferometry. The inherent incoherent properties of such illumination provided us with robustness to global illumination, yielding accurate and high-quality scene depths, and the ability to see through scattering caused by a translucent diffuser. In addition, engineering a robust optical setup helped us to mitigate most of the detrimental effects of vibrations and wind that typically reduce the quality of interferometric measurements. In the future, we plan on making reconstruction with indoor light sources much more robust by incorporating wavefront sensing and correction for near-field light sources. We hope that this work will inspire applications in fields such as high-resolution depth measurements in inspection, fabrication, robotic grasping and biomedical imaging, and extensions to passive computational light transport techniques.

REFERENCES

Supreeth Achar, Joseph R Bartels, William L Whittaker, Kiriakos N Kutulakos, and Srinivasa G Narasimhan. 2017. Epipolar time-of-flight imaging. *ACM TOG* (2017).

Girish S. Agarwal, Greg Gbur, and Emil Wolf. 2004. Coherence properties of sunlight. *Opt. Lett.* 29, 5 (Mar 2004), 459–461. https://doi.org/10.1364/OL.29.000459

Kazunori Akiyama, Katherine Bouman, and David Woody. 2019. First M87 Event Horizon Telescope Results. I. The Shadow of the Supermassive Black Hole. *Astrophysical Journal Letters* 875 (04 2019).

Brian Aull. 2005. 3D Imaging with Geiger-mode Avalanche Photodiodes. *Opt. Photon. News* (2005).

Amaury Badon, Geoffroy Lerosey, Albert C. Boccara, Mathias Fink, and Alexandre Aubry. 2015. Retrieving Time-Dependent Green's Functions in Optics with Low-Coherence Interferometry. *Phys. Rev. Lett.* 114 (Jan 2015), 023901. Issue 2. https://doi.org/10.1103/PhysRevLett.114.023901

Amaury Badon, Dayan Li, Geoffroy Lerosey, A. Claude Boccara, Mathias Fink, and Alexandre Aubry. 2016. Spatio-temporal imaging of light transport in highly scattering media under white light illumination. *Optica* 3, 11 (Nov 2016), 1160–1166. https://doi.org/10.1364/OPTICA.3.001160

Seung-Hwan Baek, Noah Walsh, Ilya Chugunov, Zheng Shi, and Felix Heide. 2021. Centimeter-Wave Free-Space Time-of-Flight Imaging. arXiv:2105.11606 [cs.CV]

Stephen T. Barnard and William B. Thompson. 1980. Disparity Analysis of Images. *IEEE TPAMI* (1980).

M. Batarseh, S. Sukhov, Z. Shen, H. Gemar, R. Rezvani, and A. Dogariu. 2018. Passive sensing around the corner using spatial coherence. *Nature Communications* 9, 1 (07 Sep 2018), 3629. https://doi.org/10.1038/s41467-018-05985-w

Jacopo Bertolotti, Elbert G Van Putten, Christian Blum, Ad Lagendijk, Willem L Vos, and Allard P Mosk. 2012. Non-invasive imaging through opaque scattering layers. *Nature* (2012).

Jeremy Boger-Lombard and Ori Katz. 2019. Passive optical time-of-flight for non line-of-sight localization. *Nature Communications* 10, 1 (26 Jul 2019), 3343. https://doi.org/10.1038/s41467-019-11279-6

Max Born, Emil Wolf, A. B. Bhatia, P. C. Clemmow, D. Gabor, A. R. Stokes, A. M. Taylor, P. A. Wayman, and W. L. Wilcock. 1999. *Principles of Optics: Electromagnetic Theory of Propagation, Interference and Diffraction of Light* (7 ed.). Cambridge University Press. https://doi.org/10.1017/CBO9781139644181

Katherine L. Bouman, Michael D. Johnson, Daniel Zoran, Vincent L. Fish, Sheperd S. Doeleman, and William T. Freeman. 2016. Computational Imaging for VLBI Image Reconstruction. *2016 IEEE Conference on Computer Vision and Pattern Recognition (CVPR)* (2016), 913–922.

R. Hanbury Brown and R.Q. Twiss. 1954. LXXIV. A new type of interferometer for use in radio astronomy. *The London, Edinburgh, and Dublin Philosophical Magazine and Journal of Science* 45, 366 (1954), 663–682. https://doi.org/10.1080/14786440708520475 arXiv:https://doi.org/10.1080/14786440708520475

R. Hanbury Brown and R. Q. Twiss. 1956. Correlation between Photons in two Coherent Beams of Light. *Nature* 177, 4497 (01 Jan 1956), 27–29. https://doi.org/10.1038/177027a0

Tongbo Chen, Hans-Peter Seidel, and Hendrik P. A. Lensch. 2008. Modulated phase-shifting for 3D scanning. In *IEEE/CVF CVPR*.

Yeou-Yen Cheng and James C. Wyant. 1984. Two-wavelength phase shifting interferometry. *Applied Optics* (1984).

Yeou-Yen Cheng and James C. Wyant. 1985. Multiple-wavelength phase-shifting interferometry. *Applied Optics* (1985).

Jon F. Claerbout. 1968. SYNTHESIS OF A LAYERED MEDIUM FROM ITS ACOUSTIC TRANSMISSION RESPONSE. *GEOPHYSICS* 33, 2 (1968), 264–269. https://doi.org/10.1190/1.1439927 arXiv:https://doi.org/10.1190/1.1439927

Oliver Cossairt. 2011. *Tradeoffs and Limits in Computational Imaging*. Ph.D. Dissertation. USA. Advisor(s) Nayar, Shree K. AAI3477396.

Matthieu Davy, Mathias Fink, and Julien de Rosny. 2013. Green's Function Retrieval and Passive Imaging from Correlations of Wideband Thermal Radiations. *Phys. Rev. Lett.* 110 (May 2013), 203901. Issue 20. https://doi.org/10.1103/PhysRevLett.110.203901

Peter de Groot. 2011. *Phase Shifting Interferometry*.

Peter de Groot and John McGarvey. 1992. Chirped synthetic-wavelength interferometry. *Optics Letters* (1992).

Yuanbo Deng and Daping Chu. 2017. Coherence properties of different light sources and their effect on the image sharpness and speckle of holographic displays. *Scientific Reports* 7, 1 (19 Jul 2017), 5893. https://doi.org/10.1038/s41598-017-06215-x

Deyan Draganov and Elmer Ruigrok. 2015. Passive Seismic Interferometry for Subsurface Imaging.

Adolf F. Fercher, H Z. Hu, and U. Vry. 1985. Rough surface interferometry with a two-wavelength heterodyne speckle interferometer. *Applied Optics* (1985).

Genevieve Gariepy, Nikola Krstajić, Robert Henderson, Chunyong Li, Robert R Thomson, Gerald S Buller, Barmak Heshmat, Ramesh Raskar, Jonathan Leach, and Daniele Faccio. 2015. Single-photon sensitive light-in-fight imaging. *Nature Comm.* (2015).

Ioannis Gkioulekas, Anat Levin, Frédo Durand, and Todd Zickler. 2015. Micron-scale light transport decomposition using interferometry. *ACM TOG* (2015).

P. Grossmann. 1987. Depth from focus. *PRL* (1987).

Anant Gupta, Atul Ingle, and Mohit Gupta. 2019a. Asynchronous Single-Photon 3D Imaging. In *ICCV*.

Anant Gupta, Atul Ingle, Andreas Velten, and Mohit Gupta. 2019b. Photon-Flooded Single-Photon 3D Cameras. In *IEEE/CVF CVPR*.

Mohit Gupta, Amit Agrawal, Ashok Veeraraghavan, and Srinivasa G Narasimhan. 2011. Structured light 3D scanning in the presence of global illumination. In *IEEE/CVF CVPR*.

Yudeog Han, Joon-Young Lee, and In So Kweon. 2013. High Quality Shape from a Single RGB-D Image under Uncalibrated Natural Illumination. In *IEEE ICCV*.

Parameswaran Hariharan. 2003. *Optical interferometry*. Elsevier.

Richard Hartley and Andrew Zisserman. 2004. *Multiple View Geometry in Computer Vision*.

Samuel W. Hasinoff and Kiriakos N. Kutulakos. 2006. Confocal Stereo. In *Computer Vision – ECCV 2006*, Aleš Leonardis, Horst Bischof, and Axel Pinz (Eds.). Springer Berlin Heidelberg, Berlin, Heidelberg, 620–634.

Caner Hazirbas, Sebastian Georg Soyer, Maximilian Christian Staab, Laura Leal-Taixé, and Daniel Cremers. 2018. Deep Depth From Focus. arXiv:1704.01085 [cs.CV]

Felix Heide, Steven Diamond, David B. Lindell, and Gordon Wetzstein. 2018. Sub-picosecond photon-efficient 3D imaging using single-photon sensors. *Scientific Reports* (2018).

Felix Heide, Matthias B Hullin, James Gregson, and Wolfgang Heidrich. 2013. Low-budget transient imaging using photonic mixer devices. *ACM TOG* (2013).

Berthold Klaus Paul Horn. 1970. *Shape from Shading: A Method for Obtaining the Shape of a Smooth Opaque Object from One View*. Technical Report.

Kamel Houairi and Frédéric Cassaing. 2009. Two-wavelength interferometry: extended range and accurate optical path difference analytical estimator. *J. Opt. Soc. Am.* (2009).

David Huang, Eric A Swanson, Charles P Lin, Joel S Schuman, William G Stinson, Warren Chang, Michael R Hee, Thomas Flotte, Kenton Gregory, Carmen A Puliafito, and James G Fujimoto. 1991. Optical coherence tomography. *Science* (1991).

R. C. Jennison. 1958. A Phase Sensitive Interferometer Technique for the Measurement of the Fourier Transforms of Spatial Brightness Distributions of Small Angular Extent. *Monthly Notices of the Royal Astronomical Society* 118, 3 (06 1958), 276–284. https://doi.org/10.1093/mnras/118.3.276 arXiv:https://academic.oup.com/mnras/article-pdf/118/3/276/8074547/mnras118-0276.pdf

Jon L. Johnson, Timothy D. Dorney, and Daniel M. Mittleman. 2001. Enhanced depth resolution in terahertz imaging using phase-shift interferometry. *Applied Physics Letters* (2001).

Moonseok Kim, Wonjun Choi, Youngwoon Choi, Changhyeong Yoon, and Wonshik Choi. 2015. Transmission matrix of a scattering medium and its applications in biophotonics. *Opt. Express* 23, 10 (May 2015), 12648–12668. https://doi.org/10.1364/OE.23.012648

Ahmed Kirmani, Tyler Hutchison, James Davis, and Ramesh Raskar. 2009. Looking around the corner using transient imaging. In *IEEE/CVF CVPR*.

Ahmed Kirmani, Dheera Venkatraman, Dongeek Shin, Andrea Colaço, Franco N. C. Wong, Jeffrey H. Shapiro, and Vivek K Goyal. 2014. First-Photon Imaging. *Science* (2014).

Alankar Kotwal, Anat Levin, and Ioannis Gkioulekas. 2020. Interferometric transmission probing with coded mutual intensity. *ACM TOG* (2020).

Robert Lange and Peter Seitz. 2001. Solid-state time-of-flight range camera. *IEEE JQE* (2001).

Robert Lange, Peter Seitz, Alice Biber, and Stefan Lauxtermann. 2000. Demodulation pixels in CCD and CMOS technologies. *SPIE* (2000).

Fengqiang Li, Florian Willomitzer, Prasanna Rangarajan, Mohit Gupta, Andreas Velten, and Oliver Cossairt. 2018. Sh-tof: Micro resolution time-of-flight imaging with superheterodyne interferometry. *IEEE ICCP* (2018).

Fengqiang Li, Joshua Yablon, Andreas Velten, Mohit Gupta, and Oliver Cossairt. 2017. High-depth-resolution range imaging with multiple-wavelength superheterodyne interferometry using 1550-nm lasers. *Applied Optics* (2017).

David B Lindell, Matthew O'Toole, and Gordon Wetzstein. 2018. Single-photon 3D imaging with deep sensor fusion. *ACM TOG* (2018).

Sheng-Hua Lu and Cheng-Chung Lee. 2002. Measuring large step heights by variable synthetic wavelength interferometry. *Measurement Science and Technology* (2002).

Heylal Mashaal, Alex Goldstein, Daniel Feuermann, and Jeffrey M. Gordon. 2012. First direct measurement of the spatial coherence of sunlight. *Opt. Lett.* 37, 17 (Sep 2012), 3516–3518. https://doi.org/10.1364/OL.37.003516

Karl Meiners-Hagen, René Schödel, Florian Pollinger, and Ahmed Abou-Zeid. 2009. Multi-Wavelength Interferometry for Length Measurements Using Diode Lasers.

Christopher A Metzler, Manoj K Sharma, Sudarshan Nagesh, Richard G Baraniuk, Oliver Cossairt, and Ashok Veeraraghavan. 2017. Coherent inverse scattering via transmission matrices: Efficient phase retrieval algorithms and a public dataset. *IEEE ICCP* (2017).

Allard P. Mosk, Ad Lagendijk, Geoffroy Lerosey, and Mathias Fink. 2012. Controlling waves in space and time for imaging and focusing in complex media. *Nature Photonics* 6, 5 (01 May 2012), 283–292. https://doi.org/10.1038/nphoton.2012.88

Lazaros Nalpantidis, Georgios Sirakoulis, and Antonios Gasteratos. 2008. Rev. of Stereo Vision Algorithms: Software to Hardware. *Int. J. Optomechatronics* (2008).

Shree K. Nayar, Katsushi Ikeuchi, and Takeo Kanade. 1990. Shape from interreflections. In *IEEE/CVF CVPR*.

Cristiano Niclass, Alexis Rochas, Pierre. Besse, and Edoardo Charbon. 2005. Design and characterization of a CMOS 3-D image sensor based on single photon avalanche diodes. *IEEE JSSC* (2005).

Matthew O'Toole, Supreeth Achar, Srinivasa G Narasimhan, and Kiriakos N Kutulakos. 2015. Homogeneous codes for energy-efficient illumination and imaging. *ACM TOG* (2015).

Matthew O'Toole, Felix Heide, David B Lindell, Kai Zang, Steven Diamond, and Gordon Wetzstein. 2017. Reconstructing Transient Images from Single-Photon Sensors. *IEEE/CVF CVPR* (2017).

Matthew O'Toole, John Mather, and Kiriakos N. Kutulakos. 2016. 3D Shape and Indirect Appearance by Structured Light Transport. *IEEE TPAMI* (2016).

Dario Piatti, Fabio Remondino, and David Stoppa. 2013. *State-of-the-Art of TOF Range-Imaging Sensors.*

SM Popoff, G Lerosey, R Carminati, M Fink, AC Boccara, and S Gigan. 2010a. Measuring the transmission matrix in optics: an approach to the study and control of light propagation in disordered media. *Physical review letters* 104, 10 (2010), 100601.

Sébastien Popoff, Geoffroy Lerosey, Mathias Fink, Albert Claude Boccara, and Sylvain Gigan. 2010b. Image transmission through an opaque material. *Nature communications* 1, 1 (2010), 1–5.

Alexis Rochas, Michael Gosch, Alexandre Serov, Pierre Besse, Rade S. Popovic, T. Lasser, and Rudolph Rigler. 2003. First fully integrated 2-D array of single-photon detectors in standard CMOS technology. *IEEE PTL* (2003).

Daniel Scharstein and Richard Szeliski. 2003. High-accuracy stereo depth maps using structured light. In *IEEE/CVF CVPR*.

Gerard Thomas Schuster. 2009. *Seismic Interferometry.* Cambridge University Press. https://doi.org/10.1017/CBO9780511581557

Rudolf Schwarte, Zhanping Xu, Horst-Guenther Heinol, Joachim Olk, Ruediger Klein, Bernd Buxbaum, Helmut Fischer, and Juergen Schulte. 1997. New electro-optical mixing and correlating sensor: facilities and applications of the photonic mixer device (PMD). In *Sensors, Sensor Systems, and Sensor Data Processing.*

Manoj Sharma, Christopher A Metzler, Sudarshan Nagesh, Oliver Cossairt, Richard G Baraniuk, and Ashok Veeraraghavan. 2019. Inverse scattering via transmission matrices: Broadband illumination and fast phase retrieval algorithms. *IEEE TCI* (2019).

Murali Subbarao and Gopal Surya. 1994. Depth from defocus: A spatial domain approach. *IJCV* (1994).

Ivo M Vellekoop and AP Mosk. 2007. Focusing coherent light through opaque strongly scattering media. *Optics letters* (2007).

I. M. Vellekoop and A. P. Mosk. 2008. Universal Optimal Transmission of Light Through Disordered Materials. *Phys. Rev. Lett.* 101 (Sep 2008), 120601. Issue 12. https://doi.org/10.1103/PhysRevLett.101.120601

Andreas Velten, Thomas Willwacher, Otkrist Gupta, Ashok Veeraraghavan, Moungi G. Bawendi, and Ramesh Raskar. 2012. Recovering three-dimensional shape around a corner using ultrafast time-of-flight imaging. *Nature Comm.* (2012).

Federica Villa, Rudi Lussana, Danilo Bronzi, Simone Tisa, Alberto Tosi, Franco Zappa, Alberto Dalla Mora, Davide Contini, Daniel Durini, Sasha Weyers, and Werner Brockherde. 2014. CMOS Imager With 1024 SPADs and TDCs for Single-Photon Timing and 3-D Time-of-Flight. *IEEE JSTQE* (2014).

Richard L. Weaver and Oleg I. Lobkis. 2001. Ultrasonics without a Source: Thermal Fluctuation Correlations at MHz Frequencies. *Phys. Rev. Lett.* 87 (Sep 2001), 134301. Issue 13. https://doi.org/10.1103/PhysRevLett.87.134301

Robert J. Woodham. 1980. Photometric Method For Determining Surface Orientation From Multiple Images. *Optical Engineering* (1980).

Liping Yan, Benyong Chen, Enzheng Zhang, Shihua Zhang, and Ye Yang. 2015. Precision measurement of refractive index of air based on laser synthetic wavelength interferometry with Edlén equation estimation. *Rev. Scientific Instruments* (2015).

Todd E Zickler, Peter N Belhumeur, and David J Kriegman. 2002. Helmholtz stereopsis: Exploiting reciprocity for surface reconstruction. *IJCV* (2002).

A IMPLEMENTATION

We discuss here implementation details of the passive interferometry setup in Figure 3(b), and a full parts list in Table 1.

Tracking the sun. When using sunlight to perform passive interferometry, the movement of the sun in the sky poses a major problem. The rotation of the earth results in an average drift of 1.25° per minute in the position of the sun. This means that with a 15 mm sensor size and a 200 mm lens with its aperture fully open, the sun passes the field of view within 20 minutes. The movement of the sun also results in significant non-uniformities in the illumination over the course of one acquisition. Therefore, it's important to track the sun and center it along the optical axis of the system every so often. We perform the tracking using two motorized precision rotation stages from Thorlabs, one for the azimuth and one for the altitude of the mirror. We control the position of these rotation stages with a PID controller, using images of the sun from an additional tracking camera focused at infinity for position feedback. In practice, we found that a proportional controller with k_p set as half the sensitivity of pixel displacements to the rotation stage angle displacements was sufficient.

Vibration isolation. As we discussed in the main paper, the most important factor detrimental to the quality of our results is vibrations in uncontrolled outdoor conditions with the interferometer built on a utility cart with no vibration isolation. To mitigate vibrations, we place our setup on a passively damped honeycomb optical breadboard from Thorlabs. We found in experiments that using the breadboard and eliminating any sources of vibrations (such as the computer in Figure 3) on the upper level of the cart is sufficient. Vibrations from the lower level of the cart do not travel to the upper level, so any noisy equipment such as the translation stage controller (the white cabinet in Figure 3(b)) can be placed on the lower level. In addition, we found that with scenes properly secured so as to not move in wind, our setup is able to tolerate winds as high as 25 mph.

Imaging camera. We use the Blackfly USB3 camera from FLIR for imaging. This camera has the high-sensitivity Sony ICX814 CCD sensor with 3380×2704 pixels, pixel size 3.5 μm, and pixel pitch 4μm. Small pixel size is important for interferometry with low spatial coherence sources, since we don't want the characteristic size of high-frequency speckle to be sub-pixel. The protective glass cover on the sensor needs to be removed, because interreflections between the two sides of the glass cover introduce two light paths, corrupting depth measurements with unwanted interference signal.

Imaging lenses. We use 200 mm prime lenses from Nikon in front of the tracking and imaging cameras to image the sun and the scene respectively. In imaging the scene, these lenses are beneficial due to their ability to achieve high magnifications, up to 1:1. In addition, these lenses are corrected for spherical aberration, which yields un-distorted depth over the entire field of view. They are also corrected for chromatic aberration, which is important because our illumination is broad-band.

Beamsplitters. We use thin plate beamsplitters from Thorlabs. The beamsplitter sending light to the tracking camera is a 10:90 (R:T)
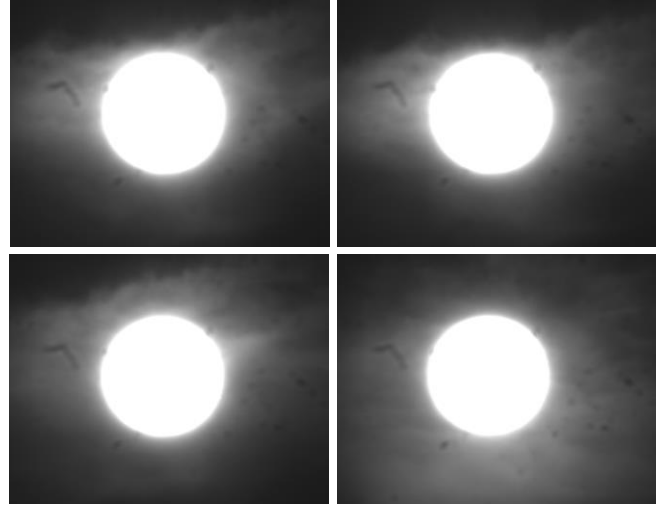

Fig. 10. Depth sensing isn't possible with heavy cloud cover. However, our method can withstand fast-moving scattered clouds. Here are four pictures of the sun imaged through the tracking camera during acquisition under moving scattered clouds.

beamsplitter, reflecting 10% of the input light to the tracking camera. The imaging beamsplitter is a 50:50 (R:T) beamsplitter. We choose plate beamsplitters over cube beamsplitters because cubes cause significant interreflections, and over pellicle beamsplitters because of their tendency to distort due to airflow.

Spectral filter. The spectra of sunlight and typical indoor light sources are very broadband, often exceeding hundreds of nanometers. This results in tiny temporal coherence lengths, requiring impractically high axial resolution reference arm scans. We place a 550±20 nm spectral filter in front of the camera to increase the coherence length to 10 μm. In practice, we found that to be enough to acquire high-quality depth. In addition to increasing coherence length, the green spectral filter helps cut out blue skylight and a large portion of ambient light coming from the indirect portion of scene illumination.

Translation stage. To ensure that we place the reference mirror at the desired positions accurately enough for micron-scale resolutions, we need a translation stage that has a minimum incremental translation less than one micron. We use the XMS160 translation stage from Newport that has a minimal incremental translation of 10 nm. In addition, this stage guarantees low-noise operation, preventing loss of interference contrast due to reference mirror position noise and by reducing vibrations.

Environmental conditions. Our experiments with sunlight were conducted under very challenging environmental conditions. For details of the location and the various problems it posed, see Figure 11.

In addition to location, availability of sunlight is a huge factor. Obviously, depth sensing with sunlight isn't possible under heavy cloud cover. However, we found that under scattered or very high-altitude clouds, we are able to obtain high-quality depth even if the clouds are fast-moving. Figure 10 shows the sun as seen from the
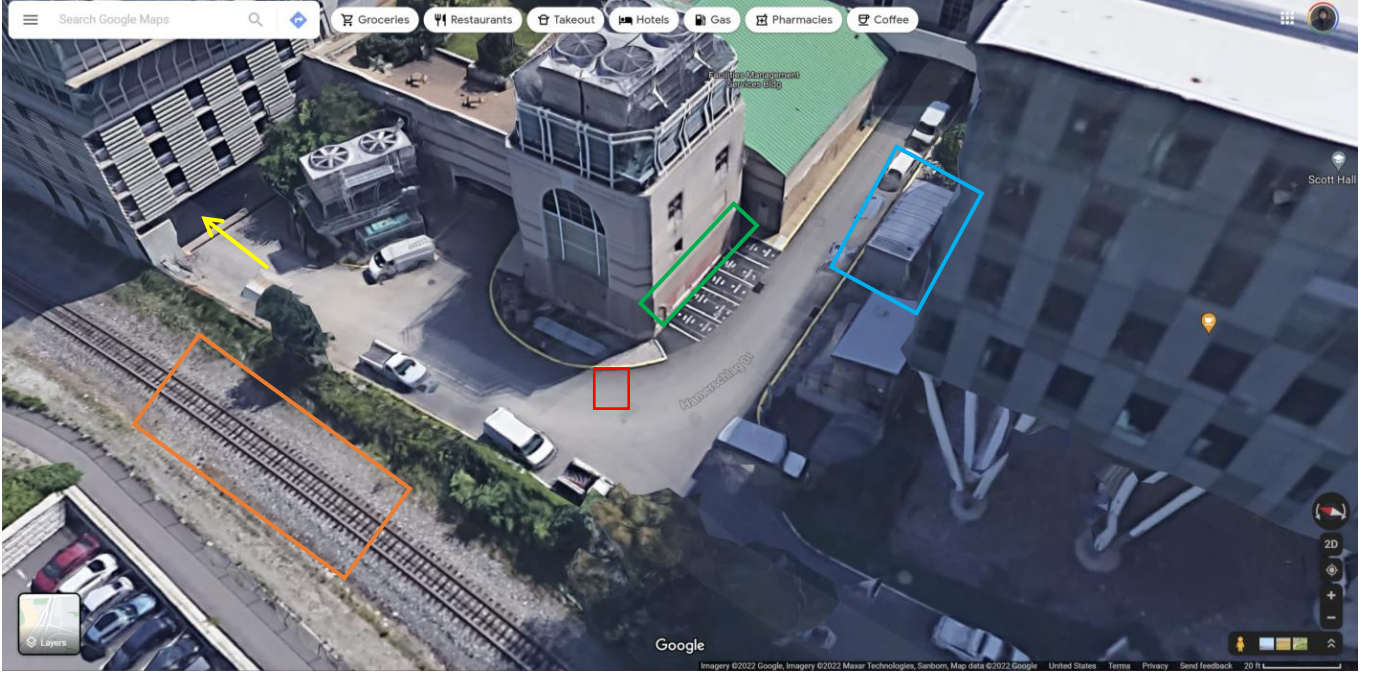
Fig. 11. Google Maps view of the site of experiments illustrating the challenging conditions our experiments were performed under. **Red**: setup location, **yellow**: parking garage, causing constant traffic with multiple vehicles, including trucks, passing per acquisition, **orange**: train tracks, with trains passing every half an hour, **green**: building air intake causing a constant background hum, **blue**: power transformer also causing a constant background hum.

tracking camera under fast-moving, scattered cloudy conditions in the span of an acquisition.

B DEPTH RENDERINGS AND SCAN FRAMES

In this section, we show the depths acquired in Figures 5 and 6 rendered as surfaces. In addition, we show some sample interference-only frames from the depth scan for each of the scenes. We have exaggerated the depth and set lighting so as to better emphasize fine features on the recovered depth map: For instance, the metal tracks on the circuit board are very clearly visible in the rendering.

C DATA AND RECONSTRUCTION CODE

To facilitate reproducibility, we make public the data captured using our passive interferometry system and the scripts used to generate results in the paper. We will also release the code used for capturing measurements and tracking the position of the sun.

In addition, Figure 14 gives some general MATLAB code for acquiring measurements from the optical setup of Figure 3(b). Figure 15 gives some code for tracking the sun in the process of acquisition, and Figure 16 gives some code for recovering direct (de-scattered) images as explained in the post-processing section of the main paper.
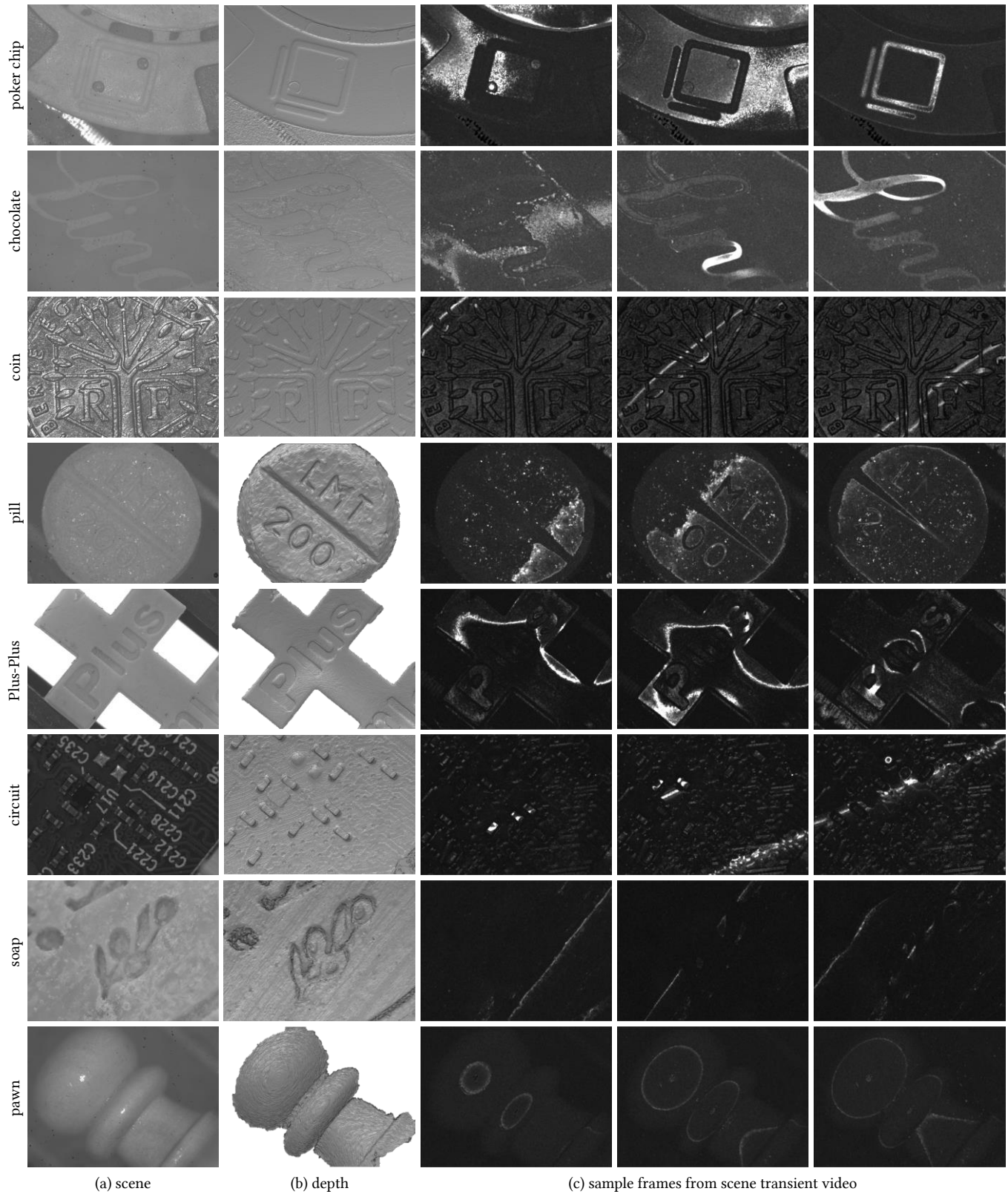
| | (a) scene | (b) depth | (c) sample frames from scene transient video |

Fig. 12. **(b)** Depth reconstruction results from Figure 5 from the main paper, rendered as 3D surfaces and **(c)** sample raw frames from the depth scans.

description	quantity	model name	company
3' × 2' utility cart	1	https://www.amazon.com/dp/B001602VI2	Rubbermaid
passively damped optical breadboard	1	B2436FX	Thorlabs
2.56" motorized precision rotation stage	1	PRMTZ8	Thorlabs
1" motorized precision rotation stage	1	PRM1Z8	Thorlabs
K-Cube brushed DC servo motor controller	2	KDC101	Thorlabs
2" round protected aluminum mirror	1	ME2-G01	Thorlabs
25 × 36 mm plate beamsplitter, 10:90 (R:T)	1	BSN10R	Thorlabs
25 × 36 mm plate beamsplitter, 50:50 (R:T)	1	BSW10R	Thorlabs
200 mm compound lens	2	AF Micro Nikkor 200mm 1:4 D IF-ED	Nikon
tracking camera	1	Grasshopper3 USB3 GS3-U3-41C6M-C	FLIR
imaging camera	1	Blackfly S USB3 BFS-U3-122S6M-C	FLIR
1" round protected aluminum mirror	1	ME1-G01	Thorlabs
2" absorptive neutral density filter kit	1	NEK03	Thorlabs
ultra-precision linear motor stage, 16 cm travel	1	XMS160	Newport Corporation
ethernet driver for linear stage	1	XPS-Q2	Newport Corporation
550 ± 20 nm bandpass spectral filter	1	FB550-40	Thorlabs

Table 1. List of major components used in the optical setup in Figure 3(b).

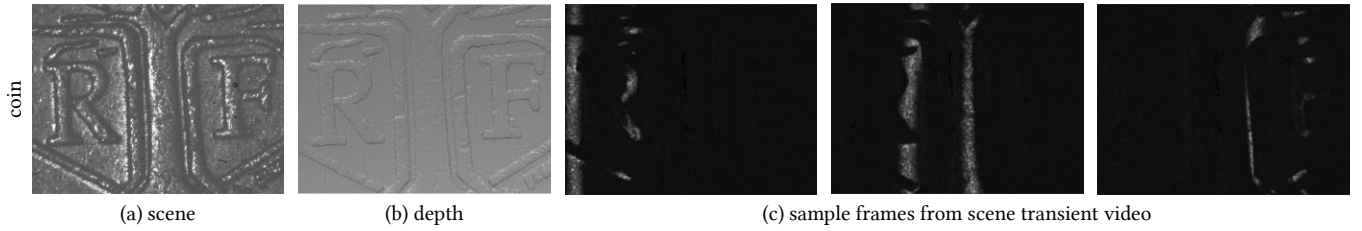(a) scene　　(b) depth　　(c) sample frames from scene transient video

Fig. 13. **(b)** Depth reconstruction result from Figure 6 from the main paper, rendered as a 3D surface and **(c)** sample raw frames from the depth scan.

```matlab
function frames = acquire(positions, imageSize, vid, refMotor, ...
                          trackingVid, trackingMotor, adjustEvery, ...
                          trackingSensitivity, trackingKp, trackingTol)

    % Acquire passive interferometry data

    % Reset motor
    refMotor.goto(positions(1));
    resolution = positions(2)-positions(1);

    % Initialize array for frames
    frames = zeros([imageSize numel(positions)], 'uint16');

    % At every position
    for i = 1:numel(positions)

        % Center the sun at every adjustEvery positions
        if mod(i, adjustEvery) == 0
            track(trackingVid, trackingMotor, trackingSensitivity, trackingKp, trackingTol);
        end

        % Record an image at this position
        frames(:, :, i) = getsnapshot(vid);

        % Translate reference arm to the next position and give it time to settle
        refMotor.translate(resolution);
        pause(0.1);

    end

end
```

Fig. 14. MATLAB code for recovering depth from our measurements

```matlab
function track(vid, motor, sensitivity, kp, tol)

    % Center the sun on the frame

    % One-dimensional tracking for brevity
    % Easily extended to two dimensions
    err = Inf;
    correction = 0;

    % Loop unless you can tolerate error
    while abs(err) > tol

        % Translate tracking motor by previous correction
        motor.translate(correction);

        % Get sun center coordinates
        image = getsnapshot(vid);
        xx = getSourceCenter(image);

        % Correct based upon the error between the image center and sun center
        err = xx-size(image)/2;
        correction = -kp*sensitivity*err;
    end

end
```

Fig. 15. MATLAB code for sun tracking

```matlab
function [depth, direct] = process(frames, positions, spatialWindow, temporalWindow)

    % Reconstruct depth from passive interferometry measurements
    % frames: HxWxN array of measurements from the camera
    % positions: set of positions of the reference arm
    % spatialWindow: blur kernel width for blurring speckle
    % temporalWindow: kernel for estimating interference-free frames

    % Convert uint16 frames from camera into double (or float in case of memory overflows)
    frames = im2double(frames);

    halfTemporalWindow = temporalWindow/2;

    % Blur `temporalWindow' frames along the positions to estimate per-position
    % interference-free images
    interferenceFree = convn(frames, ones(1, 1, temporalWindow)/temporalWindow, 'same');

    % Pad the interference-free images to remove convolution edge artifacts
    interferenceFree(:, :, 1:halfWindow) = ...
                    repmat(interferenceFree(:, :, halfWindow+1), [1 1 halfWindow]);
    interferenceFree(:, :, end-(halfWindow-1):end) = ...
                    repmat(interferenceFree(:, :, end-halfWindow), [1 1 halfWindow]);

    % Subtract interference-free images to get interference-only images
    interference = abs(frames-interferenceFree);

    % Blur with a kernel `spatialWindow' in size
    interference = imgaussfilt(interference, spatialWindow);

    % Get maximums of interference as ballistic light path image, and positions at maxima as depth
    [direct, idxs] = max(interference, [], 3);
    depth = positions(idxs);

end
```

Fig. 16. MATLAB code for acquiring measurements